Effects of Seismogenic Width and Low-velocity Zones on Estimating Slip-weakening Distance from Near-fault Ground Deformation

Xiang Chen[1] and Hongfeng Yang[1*]

[1]Earth System Science Programme, Faculty of Science, The Chinese University of Hong Kong, Sha Tin, Hong Kong, China

*Corresponding author: Hongfeng Yang (hyang@cuhk.edu.hk)

Key words: Numerical modelling; Earthquake dynamics; Dynamics and mechanics of faulting; Computational seismology, Friction.

Abstract

Fault weakening process controls earthquake rupture propagation and is of great significance to impact the final earthquake size and seismic hazard. Critical slip-weakening distance (D_c) is one of the key parameters, which however is of difficult endeavours to be determined on natural faults, mainly due to its strong trade-off with the fault strength drop. An estimation method of D_c value proposed by Fukuyama et al (2003, 2007) provides a simple and direct reference of D_c on real faults from the near-fault ground displacement at the peak of ground velocity (D_c''). However, multiple factors may affect the observed near-fault ground velocity and thus need to be considered when estimating D_c. In this work we conduct 3D finite element numerical simulations to examine the effects of finite seismogenic width and near-fault low velocity zones (LVZ) on the results of D_c''. In uniform models with constant prescribed D_c, the derived D_c'' values increase with seismogenic width. With a near-fault LVZ, D_c'' values show significant magnification. The width of the LVZ plays a more important role in enlarging D_c estimation compared to the depth of LVZ. Complex wavefields and multiple wiggles introduced by LVZ could lead to delay pick and then cause large deviation. Overestimation should be considered when using D_c'' from limited stations to infer D_c on fault. Furthermore, the scaling between D_c'' and final slip in models with a constant D_c indicates that the scale-dependent feature of D_c'' might not be related to variations in friction properties.

1 Introduction

Earthquakes occur when fast slip develops on faults, which has been widely attributed to fault strength weakening. The significant strength reduction with fault slip and slip rate growth was revealed by both laboratory experiments and seismological observations (Wibberley and Shimamoto, 2005; Di Toro et al., 2011; Goldsby and Tullis, 2011; Houston, 2015; Viesca and Garagash, 2015). Multiple mechanisms have been proposed to cause the coseismic strength weakening, such as thermal pressurization, powder lubrication, flash heating and so on (Reches and Lockner, 2010; Goldsby and Tullis, 2011; Viesca and Garagash, 2015). To depict the strength decline process, a linear slip-weakening law was introduced (Ida, 1972) and had been pervasively used in physical-based earthquake simulations (D J Andrews, 1976; Day, 1982; Olsen et al., 1997; Dunham and Archuleta, 2004; Ma et al., 2008; Yang et al., 2013; Weng et al., 2016; Weng and Yang, 2018), in which the fault strength drops linearly from static friction to dynamic friction during a portion of slip, known as slip-weakening distance D_c. Tremendous efforts have been made to unravel the riddles of fault weakening process. However, determining the value of slip-weakening distance D_c on natural faults is still a difficult endeavor.

Various attempts have been made and provide basic constraints on D_c and other dynamic source parameters (Bouchon, 1997; Ide and Takeo, 1997; Nielsen and Olsen, 2000; Dalguer et al., 2002; Fukuyama, 2003; Mikumo et al., 2003; Tinti et al., 2005a, 2005b; Ma et al., 2008; Weng and Yang, 2018; Yao and Yang, 2020). Kinematic source inversions place well constraints on slip distribution during earthquakes. Slip history on each grid of the fault plane was then derived to determine stress evolution so as to estimate the D_c from the slip-stress history. Such approach was first applied to the 1995 Kobe earthquake from which a depth-dependent D_c distribution was claimed (Ide and Takeo, 1997). More earthquakes were investigated by this approach (Bouchon, 1997; Tinti et al., 2005b). However, kinematic inversion estimation may be limited by resolution and thus biased by factors such as the adoption of source time function and limited bandwidth (Spudich, 2005). In comparison, dynamic rupture simulations solve the stress history spontaneously and do not depend on the slip-stress results from kinematic inversions. However, how to obtain reasonable initial conditions is challenging and strong trade-off between slip-weakening distance and the strength reduction existed (Guatteri, 2000; Goto and Sawada, 2010). Recently, the non-uniqueness in dynamic source parameters could be diminished by using multiple near-field observations (Weng and Yang, 2018; Yang and Yao, 2019).

An estimation method of D_c value proposed by Fukuyama and Mikumo provides a simple and direct reference of slip-weakening distance on real faults (Fukuyama, 2003; Mikumo et al., 2003; Fukuyama and Mikumo, 2007), based on the proximity between the traction breakdown time and peak slip rate time in the condition of relatively smooth rupture development. When the rupture propagates smoothly, D_c on the ruptured fault, could be approximated by observations at surface stations on fault at the time of the maximum slip rate (${D_c}'$) (Fukuyama, 2003; Mikumo et al., 2003). For off-fault stations, twice of fault-parallel displacement at the time of peak ground velocity, ${D_c}''$, was defined as an approximation of the D_c in strike-slip faults (Fukuyama and Mikumo, 2007). Therefore, observations at near-fault seismic and geodetic instruments enable a fast estimation of the slip-weakening parameter.

However, near-fault coseismic observations are affected by several factors such as low-velocity fault damage zones (Ben-Zion and Sammis, 2003) and seismogenic width (Weng and Yang, 2017). Damage zones are pervasively distributed along crustal faults and are characterized by low seismic velocity (velocity reduction around 20%-50%), usually with a width of hundreds to thousands meters (Yang and Zhu, 2010; Yang et al., 2011, 2014; Yang, 2015; Yang et al., 2020). The existence of damage zone could not only promote the earthquake ground motion amplitude (Ben-Zion and Aki, 1990; Wu et al., 2009; Kurzon et al., 2014; Yang, 2015), but also impact earthquake rupture development (Huang and Ampuero, 2011; Weng et al., 2016). Since the ${D_c}''$ method relies on near-fault observation, the near-fault damage zone, also called low-velocity zone (LVZ), could affect the estimation of D_c.

Moreover, a recent study obtaining slip-weakening distance from D_c'' method suggests the scale-dependence of D_c'' with earthquake final slip (Fukuyama and Suzuki, 2016; Kaneko et al., 2017) . While according to recent numerical studies, even without the difference in weakening parameters and stress distribution, only variation in seismogenic width would lead to change in earthquake moment (Weng and Yang, 2017). Furthermore, the final earthquake moment may be subjected to hypocentral location and heterogeneous stress distribution although the D_c is uniform on the fault (Yang et al., 2019). In order to examine the foregoing factors and effects on D_c estimation, we conduct numerical simulations to investigate the above questions, for a better understanding of near-fault ground deformation and how the estimation of D_c may be affected.

2 Model and Method

In this study, we use finite element code PyLith (Aagaard et al., 2013) to run 3D dynamic rupture simulations. The spontaneous rupture is governed by a linear slip-weakening friction law (Ida, 1972) shown in equation (1):

$$\tau(\delta) = \begin{cases} \tau_s - \dfrac{(\tau_s - \tau_d)\delta}{D_c} & \delta \le D_c \\ \tau_d & \delta > D_c \end{cases}. \quad (1)$$

τ_s, τ_0 and τ_d denote the static frictional strength, initial shear stress and dynamic stress on fault plane, respectively (Table 1). A uniform slip-weakening distance, D_c is set to be 0.4 m, which falls within the range of values that numerical simulations typically select (Day et al., 2005; Bizzarri et al., 2010; Weng and Yang, 2017).

We set a vertical planar strike-slip fault imbedded in a $120 \times 36 \times 30\ \mathrm{km}^3$ domain, in which all boundaries are absorbing boundaries except the free surface on the top (Fig. 1a). In our models, the ruptures are allowed to propagate to the surface, as the ground velocity of buried-fault rupture may not contain enough information about the slip-weakening distance (Cruz-Atienza et al., 2009). The fault plane extends 100 km in along-strike length. We select variant seismogenic widths (w) in depth to investigate their effects.

To initiate the spontaneous rupture, we introduce a circular prestressed nucleation zone in the middle of the seismogenic width, within which the initial shear stress, τ_0^{i} is slightly higher than the static strength τ_s (Table 1). A proper selection of nucleation zone size should ensure a stable rupture development, shorten the initiation time but also decrease the artificial effect (Bizzarri 2010, Galis *et al.* 2015). The radius of circular nucleation zone in this study is 4.0 km, which by test could establish stable rupture propagation in the current stress and friction level and also satisfies the estimated critical nucleation threshold (Galis et al., 2015):

$$\mathrm{R_{nuc}} = \frac{\pi}{4}\frac{1}{f_{min}^2}\frac{\tau_s - \tau_d}{(\tau_0 - \tau_d)^2}\mu D_c. \quad (2)$$

$\mathrm{R_{nuc}}$ refers to the critical nucleation zone radius of breakaway rupture, and f_{min} is the minimum of the function:

$$f(x) = \sqrt{x}\left[1 + \frac{\tau_0^i - \tau_0}{\tau_0 - \tau_d}\left(1 - \sqrt{1 - 1/x^2}\right)\right] \quad (3)$$

where τ_0^i is the initial shear stress inside the nucleation zone. Appling the values in Table 1, $f_{min} \approx 1.626$ and the critical nucleation size is $\mathrm{R_{nuc}} \approx 3.92$ km. Our selection of nucleation radius $\mathrm{R_{nuc}}$= 4.0 km just meets the requirement of critical nucleation size to ensure a continuous propagation on the entire fault thus we could calculate the D_c'' with smooth rupture propagation.

In the simulations with low-velocity zones, we set a finite low-velocity region confined by L_d in depth and L_w in the fault-normal direction (Fig. 1b). The velocity reductions observed at different faults range from ~20%-50% (Yang, 2015). Here the velocity reduction is set at a fixed value 30%, i.e. $\frac{\mathrm{V_p - V_{p,L}}}{\mathrm{V_p}} = \frac{\mathrm{V_s - V_{s,L}}}{\mathrm{V_s}} = 30\%$, in which $\mathrm{V_p}, \mathrm{V_s}$ represent the P and S wave velocities in the surrounding rocks (same as that in homogeneous model, shown in Table 1), while $V_{p,L}, V_{s,L}$ refer to the P and S wave velocities in the LVZ, respectively. For simplicity, we set uniform density in the whole model.

Calculating D_c'' demands good spatial and temporal resolution near the passage of rupture tips. To achieve a good spatial resolution in rupture tips and a convergent numerical result requires three or more grids inside the cohesive zone (Day et al., 2005). Cohesive zone refers to the area behind rupture tip where shear stress decrease from peak strength to dynamic friction. An estimation of the static cohesive zone length for linear slip-weakening law is given in equation (4) (Palmer and Rice, 1973; Day et al., 2005):

$$\Lambda_0 = \frac{9\pi}{32}\frac{\mu}{1-\nu}\frac{D_c}{\tau_s - \tau_d}. \quad (4)$$

The grid size is $\Delta x = 200\,m$ in all models. Substituting the material property parameters in Table 1 into equation (4), for homogeneous models $\Lambda_0/\Delta x \approx 16$, while for the low-velocity zone with 30% velocity reduction $\Lambda_0/\Delta x \approx 7$, both meeting the numerical requirements. We also conduct convergence tests using grid size of 150 m and 250m. The slip distribution and slip rate on fault indicate that the numerical solutions are well converged for the grid sizes of 150 m and 200 m (Fig. S1). Comparison of ground velocities from models of different grid sizes also confirm that our choice of 200 m is sufficiently small to resolve the rupture process in our models (Fig. S2). The selection of time interval is $\Delta t = 0.01s$ in this study, which satisfies the Courant-Friedrichs-Lewy law (Courant et al., 1928) that the Courant-Friedrichs-Lewy ratio $CFL = V_p \Delta t/\Delta x < 0.71$.

3 Data Processing and Results

We nucleate ruptures at $x = 0$ and output ground velocities and displacements from each dynamic rupture scenario (Fig. 2a). In the homogeneous model ($w = 15\ km$), if we track one point on the fault plane, the traction breakdown time and slip history indicate that D_c is 0.4 m (Fig. 2b), as we defined. For the record at the surface (Fig. 2c), D_c' is measured at the time when slip rate on fault reaches the peak value (Mikumo et al., 2003, Fukuyama et al. 2003). Similarly, a D_c'' value is inferred at a station that is 0.2 km away from the fault at the time when fault-parallel velocity (FP velocity) reaches the maximum (Fig. 2d). By far this method has been applied on a few earthquakes (Table 2). Due to the limited instrument coverage, it is uncommon to have near-fault records that capture the coseismic ground motion. In the existing cases (Table 2), near-fault seismic stations distribute from the ruptured faults with distances of 0.1 km to 3 kms. In our numerical simulations, we calculate and analyze D_c'' in one quadrant on the ground surface in distance up to 3 km, according to the observations.

3.1 Effects of filtering and coherency of ground velocities on estimating D_c''

To obtain consistent and reliable D_c'' value, we need to pre-process the fault-parallel ground velocity data output from model simulations. The peak velocity time directly inferred from the raw data may be affected by the high-frequency spikes in simulated waveforms. For instance, the peak velocity time on the raw data is slightly advanced comparing with that from the lowpass filtered data (Fig. 2d). In addition, the peak value is very close in the next wiggle and thus if we track the peak value in the raw data, we may obtain fluctuated D_c'' distribution (Fig. 3a). As the high-frequency contents in the waveforms appear to depend on the grid size (Fig. S2), they are likely numerical noise and do not represent the accurate synthetic ground velocities. As such, we apply a lowpass filter to remove the high-frequency wiggles in ground velocity data and obtain stable D_c'' values after applying a 2 Hz zero-phase lowpass filter (Fig. 3b). Comparing to the D_c'' results obtained from raw data (Fig. 3a), random values with large deviations from the true D_c value are removed (Fig. 3b).

In order to pick stable and continuous time moments automatically, we need to select a reasonable frequency range for the synthetic data. To test the potential bias introduced by filter, we check the frequency effects from 0.5 Hz to 3 Hz on ground velocity. For ground velocity waveform from homogeneous model ($w = 15\ km$), decreasing cutoff frequency would cause slight delay of peak velocity time (Fig. 4a) and thus leads to overestimation of D_c'' with lower cutoff frequency. To remove all the local wiggles but keep the shape of ground velocity pulse as much as possible, we chose 2 Hz as the cutoff frequency and apply it to all the models. Comparison of D_c'' values with different lowpass filters shows that the D_c'' values become stable for cutoff frequency up to 2 Hz (Fig. 4b - d). For most of the grids, D_c'' difference introduced between 2 Hz and 3 Hz filter is less 0.05 m (Fig. 4b).

In addition to the effects of filtering, we find that inconsistent phase picking at off-fault locations may also play a role in estimating the D_c'' values. Previous studies get D_c'' at the time of the maximum ground velocity (Fukuyama and Mikumo, 2007; Fukuyama and Suzuki, 2016; Kaneko et al., 2017). However, our synthetic ground velocity shows that latter phase may exhibit larger amplitude (Fig. 3d, shown as light green ticks on filtered waveforms). When using the absolute maximum velocity value to mark the passage of rupture front, inconsistent phases may be used to mark D_c''(Fig. 3d). In simulation, we have the advantage to set numerous virtual stations to obtain the D_c'' from the consistent phases; so we track the consistent phases to mark D_c'' from the location above nucleation center ($x = 0$) and obtain the D_c'' distribution from coherent phases (Fig. 3c & d).

To obtain D_c'' values from consistent velocity phase, we use the following criterion to pick the first main peak velocity related with rupture front. For the ground grids nearest to the fault, the shape of velocity waveform is a clear single pulse, and we track the maximum velocity as t_p (peak velocity time corresponding to D_c'') from the initial center along the fault strike. For other ground grids, we search the first local maximum velocity within a 3-second time window according to the t_p of its most adjacent grid closer to the fault. We take this time moment as the rupture-related peak velocity time, t_p, of the grid so as to mark the corresponding displacement as D_c''. The purpose of setting a search window is to track the first rupture-related phase and avoid the deviation caused by multi-wiggles and potential multi-rupture phases. Animation of fault slip rate and fault-parallel ground velocity (Supplementary animation SM1) development has been inspected to confirm that our selected first peaks are related to the passage of rupture fronts.

After correcting coherency in phase picking, the D_c'' values appear to be mostly underestimated (Fig. 3c). Before we pick coherent phases, there is a zone with fault-normal distance less than ~1 km with overestimated values (Fig. 3a & b). In addition, such overestimations become severe in a region with fault-normal distance up to 3 kms with along-strike distances of ~10-22 km (Fig. 3a & b), corresponding to the initial stage of the rupture that nucleated from x = 0. Although such overestimations are removed by picking coherent phases, in the area associated with initial rupture stage the D_c'' values are significantly underestimated (Fig. 3c). Thus we only use the region where stable rupture is established on fault in the following statistics. We use the D_c'' values on the ground surface in a 20 km (along-strike) × 3 km (fault-normal) area. The range in along-strike direction is 25~45 km from the nucleation zone. The selection in fault normal direction of 3 km is based on the largest off-fault distance of stations (3 km, Table 2) used to obtain D_c'', in the 2002 Denali earthquake (Fukuyama and Mikumo, 2007).

3.2 D_c'' values of homogeneous bounded-seismogenic fault

As investigated by recent study (Weng and Yang, 2017), the width of seismogenic fault may affect the rupture development and the final earthquake scale. So we conduct simulations with variant seismogenic widths to evaluate the effects on D_c'' values. We show the D_c'' distribution of uniform models with seismogenic width ranging from 10 km to 20 km (Fig. 5), which is typical for crustal strike-slip faults. These models with different seismogenic widths have constant $D_c = 0.4\,m$ and all other parameters as the same (Table 1). The outputted fault-parallel ground velocities are processed by the above procedure with filtering and coherency correction. The obtained D_c'' on the ground is shown as deviation degree from prescribed D_c (i.e. $\frac{D_c''-D_c}{D_c}$).

In general, D_c'' increases with seismogenic width (Fig. 5). After coherency correction for models with narrower seismogenic width, especially $\mathrm{w} \leq 15\ \mathrm{km}$, D_c'' underestimates the real D_c for most grids in the selected area. In the model with $\mathrm{w} = 10\ \mathrm{km}$, the largest D_c'' deviation is around 57% from prescribed D_c in the near-fault region of stable rupture segment. Overestimating appears as seismogenic width gets larger, which mainly occurs in the region further away from the fault trace, especially in the model with $\mathrm{w} = 20\ \mathrm{km}$ (Fig. 5e). The large D_c'' values in the zone of ~2 grids from fault is produced by the waveform change from single pulse to double peaks of fault-parallel velocity. We calculate the average D_c'' in the selected area and find a linear increasing trend (Fig. 6a), although the prescribed D_c on fault is a constant. Standard variation of D_c'' ranges from 0.1～0.2 m for $D_c = 0.4\ m$.

As the D_c'' is determined by the shape and integral of fault-parallel velocity, we compare the velocity waveforms from models with different seismogenic widths on the ground surface. We extract fault-parallel velocity waveforms from same ground location and align them at the selected peak time t_p (Fig. 6b). Amplitudes of the selected velocity peaks increase significantly with seismogenic width, but the time durations before reaching the peaks are similar (Fig. 6b), which leads to growing integral values at time t_p, i.e. D_c''. In comparison, the slip rate on fault shows the similar features as ground velocity, with peak values increasing with seismogenic widths while time durations are similar (Fig. 6c).

Such difference is attributed to stress reduction rate, which is faster for models with larger seismogenic widths (Fig. 6d). According to Day, 1982, strain rate released at rupture tip could be approximated by:

$$G \approx \frac{\pi}{2}\left(\frac{V_S}{V_R}\right)^2 \frac{\mathcal{R}(V_R)}{\sqrt{1-\frac{{V_R}^2}{{V_S}^2}}} \cdot \frac{\Delta\tau^2}{\mu} w \quad (5)$$

in which V_R is the rupture speed, $\mathcal{R}$ is the Rayleigh function ($\mathcal{R}(c) = [\sqrt{1-\frac{c^2}{V_P{}^2}}\sqrt{1-\frac{c^2}{V_S{}^2}} - (1-\frac{c^2}{2V_S{}^2})^2]$), $\Delta\tau = \tau_0 - \tau_d$, and w is the seismogenic width. Thus, the stress reduction rate depends on the widths. For the fault grids shown in Fig. 6d, peak velocity time (shown as dots in Fig. 6d) arrives earlier than stress breakdown time. Thus, the deviation occurs with on-fault $D_c{}'$ (shown in supplementary S3). As seismogenic width decreases, the advance in time of peak velocity than the stress breakdown time gets larger, which explains why the $D_c{}''$ underestimation gets more significant at narrower seismogenic width.

Along the fault-normal direction, waveforms distort from impulsive forms (with single peak) to ramp-like forms (with multiple wiggles) as away from the fault surface (Fig. 7a), which is responsible for the coarse $D_c{}''$ distribution in that direction (Fig. 7b). In the transition zone of waveform change, the effects on $D_c{}''$ is complicated. For the off-fault grids where shape change impends ($y = 0.4\ km$ in Fig. 7b), the latter wiggle grows into undistinguishable with the first pulse and cause a widen velocity pulse and thus delayed peak time t_p, leading to large $D_c{}''$ values at t_p. Further away from fault ($y = 0.6\ km$ in Fig. 7b), $D_c{}''$ decreases quickly once the multi-wiggle shape is formed. Then $D_c{}''$ increases gradually with fault-normal distance as the velocity waveform gets wider (Fig. 7a). The $D_c{}''$ variation related to waveform distortion could be around 15-50% in the transition zone (Fig. 8). Except in this region, the $D_c{}''$ values at both the nearest and away from fault distance show positive correlation with seismogenic width.

3.3 $D_c{}''$ values of models with LVZ

Around the seismogenic fault surface, we set the LVZ (Fig. 1b) to investigate the $D_c{}''$ values when there is a near-fault damage zone. In Fig. 9 we show the $D_c{}''$ and waveforms on the ground of a LVZ model in which a 2.4 km-wide L_w and 3 km-deep L_d low-velocity zone with 30% velocity reduction is inserted around the fault plane. With the existence of low-velocity zone, $D_c{}''$ values appear to overestimate the D_c, because ground velocities and displacements are amplified by the LVZ. After filtering and correcting coherency, D_c'' values from the LVZ model (Fig. 9a) are larger than twice of D_c'' in the homogeneous model (Fig. 3c), especially near the fault trace. Besides, enlargement of D_c'' not only occurs within the LVZ zone (Fig. 9a). It affects a broader area beyond the low-velocity range. After coherency corrections, the overestimate could be more than 100% in the near-fault region (Fig. 9a).

Moreover, the LVZ leads to multiple wiggles and more complex wavefields in the near-fault ground velocity (Fig. 9c & d). Furthermore, the later seismic phase might have larger amplitude than the first rupture related phase (shown as light green and blue ticks respectively in Fig. 9c & d), leading to overestimates of real D_c when estimating D_c'' at the maximum velocity time (Fig. 9b). The deviation degree from real D_c could be larger than 200% in near-fault regions if we do not follow the coherent phase (Fig. 9b).

Moreover, geometric structure of LVZ varies for different fault systems. To investigate the effects from LVZ geometry, we change the LVZ width (L_w) from 1.2 km ~ 2.4km, depth (L_d) from 1.0 km to 5.0 km and calculate the average D_c'' of the selected area using the first rupture related phase (Fig. 10a). By changing geometry of the LVZ, we find the width of the LVZ has a pronounced promotional effect on D_c'' values. The D_c'' values show positive correlation with LVZ width (L_w) for each L_d (Fig. 10). However, the increase of LVZ depth (L_d) does not always significantly promote the average D_c'' value. This might be related to the competing effects brought by increasing L_d. In one side, larger L_d expands the region of LVZ and magnifies the D_c''; on the other hand, extending of LVZ depth lowers the rupture speed on fault plane, which might contribute to the decrease of D_c'' (Supplementary SM2 shows a rupture development movie of a LVZ model). Meanwhile, the calculated D_c'' using the maximum velocity phase in LVZ models (similar to Fig. 9b) show the same increasing pattern with L_w but much larger average values (Fig. 10b). We also conduct simulations with different velocity reduction value (40%). The effects from velocity reduction values are minor, and variation pattern from LVZ geometry maintains the same at different velocity reduction values. The results with a LVZ highlight the importance of understanding fault zone structures when using the D_c'' method to infer D_c in real cases.

4 Discussion

4.1 Off-fault distance and resolution distance R_c

In Cruz-Atienza *et al.* 2009, a resolution distance R_c is proposed for reasonable D_c'' estimation, which could be estimated by $R_c \approx 0.8V_sT_c$. V_s is shear wave speed, and T_c refers to the time span of stress breakdown process. In our homogeneous models, $V_s = 3.33\ km/s$ and T_c is around 0.5 s, despite the variation in different positions and different models. Substitution into the equation, we get $R_c \approx 1.3\ km$ for homogeneous model, and smaller values for models with LVZ.

On the other hand R_c could be approximated by the cohesive zone length. The cohesive length varies in depth and time. An average value in the middle depth of the corresponding fault segment is around $1{\sim}1.2\ km$. In previous sections we analyze the waveforms and D_c'' values within 3 km off-fault distance. The choice of the off-fault range is meant to show the D_c'' values in a broad region based on the current application of D_c'' method, in which the largest off-fault distance is 3 km in Denali earthquake (Fukuyama and Mikumo, 2007). A narrower off-fault range would not change the obtained variation trend (Fig. 6a). The mean D_c'' values obtained in the nearest grids still present an increasing trend with seismogenic width (shown as crosses in Fig. 6a). In Fig. 6b we show the ground velocity waveforms of nodes with nearest off-fault distance (off-fault distance = 0.2 km) and the corresponding D_c'' values. The increasing tendency of D_c'' with seismogenic width still holds.

4.2 D_c'' and velocity waveforms in fault-normal direction

As ruptures propagate smoothly in the selected area, along strike direction the waveforms show high consistency and D_c'' values are continuous with minor variations in uniform models. In the fault-normal direction, D_c'' presents a piecewise variation pattern as described in section 3.2 (Fig. 7 & 8). The pattern indicates that in the near-field off-fault region, more complex D_c'' values might appear due to the waveform shape change.

The off-fault variation of D_c'' is also calculated in other 3D spontaneous rupture simulations (Cruz-Atienza *et al.* 2009), in which an increasing trend is shown within around 2 km, different from the features in our results shown in Fig. 7 & 8. The near fault complexity in Fig. 7 originates from the waveform shape change as off-fault distance increases, which does not appear in Cruz-Atienza *et al.* 2009. The inconsistency might be related to the difference in profile location. The fault-normal profile in previous study to show variation in D_c'' values is directly above the nucleation center, while we show the average value in an area where rupture propagates tens of kilometers out of the nucleation zone. The selection in this study intends to avoid the effects from artificial initial zone and to calculate D_c'' at positions where rupture grows stably, as shown in Fig. 3. Even though selecting an area in middle part of the rupture may contain the effects of rupture propagation history, it is a more general choice which diminishes the potential impact from different strategies in rupture initiation.

4.3 Scale dependence of D_c''

In the current application of D_c'' on real earthquakes, the earthquake magnitudes range from M_w 6.6 to M_w7.9, with an order of difference in maximum slip (Table 2). As a results, D_c'' increases with slip linearly (Fukuyama and Mikumo, 2007; Fukuyama and Suzuki, 2016; Kaneko et al., 2017). In our models, the average D_c'' values also increase with slip, e.g. in the models with different seismogenic widths (Fig. 11). As the seismogenic widths may affect the moments even with homogeneous parameters (Weng and Yang, 2017), such results are well anticipated because D_c'' here is essentially near-field displacement, which is scaled to moment and moment rate (Aki and Richards, 2002). However, the prescribed D_c is a constant (i.e. 0.4 m) in all our models, indicating that the scale dependence of D_c'' with slip/moment can not reflect that D_c must be scaled with slip.

Whether dynamic source parameters such as D_c are scale-dependent has been widely investigated in previous studies (Abercrombie and Rice, 2005; Tinti et al., 2005a, 2005b, 2009; Cocco and Tinti, 2008; Viesca and Garagash, 2015). The scale-dependent fracture energy from seismological observation might provide indirect constrains on the increasing trend of D_c with earthquake slip (Abercrombie and Rice, 2005; Tinti et al., 2005b; Cocco and Tinti, 2008; Viesca and Garagash, 2015), which however still contains uncertainties due to the trade-off between D_c and strength excess. Although recent studies have removed the trade-off using near-field observations and kinematic sources parameters (Weng and Yang, 2018; Yao and Yang, 2020), it is extremely challenging to distinguish whether D_c is homogeneous or heterogeneous in the condition of heterogeneous stress distribution (Yao and Yang, 2020).

4.4 Potential deviation of D_c'' estimation

Utilizing the advantages of numerical simulation, we set numerous of virtual stations on the ground and obtain the average D_c'' using the coherent velocity phase in the stable rupture segment. However, in reality, it is uncommon to have more than one station in the near-fault region (i.e. less than 3 km to the ruptured fault) to capture the coseismic deformation. Therefore, D_c'' is likely inferred from the maximum velocity without coherence correction, as did in previous studies (Fukuyama and Mikumo, 2007; Fukuyama and Suzuki, 2016; Kaneko et al., 2017). As shown in our numerical results, overestimations could be as large as 70% and increase with seismogenic width. If there is a profound LVZ surrounding the ruptured fault, D_c'' obtained at the maximum ground velocity is significantly amplified (Fig. 9b & 10b). The overestimation bias at single location could be as large as twice of the real D_c (Fig. 9b). The near-field complexity requires multiple stations to achieve better estimation of D_c. Recently, with the increasing deployment of near-fault dense arrays, more near-fault waveform data would become available and provide opportunities to obtain more D_c'' measurements.

Besides seismogenic width and near-fault low velocity zone, there are other potential factors which could play roles in the D_c'' estimation. For example, in this study we use uniform stress distribution in models; as the heterogeneity would leads to heterogeneous slip distribution, it may affect the on-fault D_c' and D_c'' on the ground. Another important factor is the rupture speed. As D_c'' is mainly obtained from strike-slip faults, effects from supershear rupture needs to be considered. One of the four current application cases, Denali earthquake (Table 2), is considered to have supershear rupture speed. From numerical simulations, transient or stable super shear rupture is suggested to be a common phenomenon with the rupture reaches free-surface (Kaneko and Lapusta, 2010; Xu et al., 2015). In supplementary figure S4, we show the results from different S ratio ($S = \frac{\tau_s - \tau_0}{\tau_0 - \tau_d}$) (D. J. Andrews, 1976) as S ratio impact the rupture speed and occurrence of supershear rupture. In a bounded fault, the S ratio would also affect rupture transition from breakaway to self-arresting (Weng and Yang, 2017). Thus, the effects of S ratio and rupture speed might be significant and thus may demand additional work to investigate.

5 Summary

We conduct numerical simulations of 3D spontaneous rupture to investigate the estimation results of D_c using D_c'' values, regarding the effects from seismogenic width and low-velocity zones. We picked the first rupture-related peak from lowpass filtered ground velocity and obtained D_c'' from the ground displacements within a selected area where stable rupture is established. With a constant prescribed D_c on homogeneous fault, the obtained D_c'' from the ground surface shows positive correlation with seismogenic width, as the amplitude of ground velocity increases with the width. With the existence of LVZ, the ground velocity is amplified and complicated with multi-wiggles, and the corresponding D_c'' is magnified. The complex wavefields introduced by the LVZ might lead to large overestimation when using D_c'' at the maximum velocity time to estimate D_c. The width of LVZ plays a more prominent effects on enlarging D_c'' compared to LVZ depth. The numerical results indicate that the obtained scale dependence based on D_c'' might be affected by the effects of fault geometry and material properties, such as seismogenic zone width and low-velocity zone. Overestimation should be considered when using D_c'' from limited near-fault stations to infer D_c on real fault.

Acknowledgements:

This study is supported by Hong Kong Research Grant Council Grants (14313816, 14306418), CUHK Direct Grant from Faculty of Science, China Earthquake Science Experiment Project, CEA (grants no. 2017CESE0103, 2018CSES0102), and State Key Lab of Earthquake Dynamics (grant no. LED2017B07), Institute of Geology, CEA. The figures are made by using Generic Mapping Tools (GMT). We appreciate constructive comments from Pierre Romanet and an anonymous reviewer.

References

Aagaard, B.T., Knepley, M.G., & Williams, C.A., 2013. A domain decomposition approach to implementing fault slip in finite-element models of quasi-static and dynamic crustal deformation, *J. Geophys. Res. Solid Earth*, **118**, 3059–3079.

Abercrombie, R.E., & Rice, J.R., 2005. Can observations of earthquake scaling constrain slip weakening?, *Geophys. J. Int.*, **162**, 406–424.

Aki, K., & Richards, P.G., 2002. Quantitative seismology, 2nd ed, *University Science Books*, Sausalito, CA.

Andrews, D J, 1976. Rupture Velocity Of Plane Strain Shear Cracks., *J Geophys Res*, **81**, 5679–5687.

Andrews, D. J., 1976. Rupture propagation with finite stress in antiplane strain, *J. Geophys. Res.*, **81**, 3575–3582.

Ben-Zion, Y., & Aki, K., 1990. Seismic Radiation From an S H Line Source in a Laterally, *Bull. Seism. Soc. Am*, **80**, 971–994.

Ben-Zion, Y., & Sammis, C.G., 2003. Characterization of fault zones, *Pure Appl. Geophys.*, **160**, 677–715.

Bizzarri, A., 2010. How to promote earthquake ruptures: Different nucleation strategies in a dynamic model with slip-weakening friction, *Bull. Seismol. Soc. Am.*, **100**, 923–940.

Bizzarri, A., Dunham, E.M., & Spudich, P., 2010. Coherence of Mach fronts during heterogeneous supershear earthquake rupture propagation: Simulations and comparison with observations, *J. Geophys. Res. Solid Earth*, **115**, 1–22.

Bouchon, M., 1997. The state of stress on some faults of the San Andreas System as inferred from near-field strong motion data, *J. Geophys. Res. Solid Earth*, **102**, 11731–11744.

Cocco, M., & Tinti, E., 2008. Scale dependence in the dynamics of earthquake propagation: Evidence from seismological and geological observations, *Earth Planet. Sci. Lett.*, **273**, 123–131.

Courant, R., Friedrichs, K., & Lewy, H., 1928. Über die partiellen ifferenzengleichungen der mathematischen Physik, *Math. Ann.*, **100**, 32–74.

Cruz-Atienza, V.M., Olsen, K.B., & Dalguer, L.A., 2009. Estimation of the breakdown slip from strong-motion seismograms: Insights from numerical experiments, *Bull. Seismol. Soc. Am.*, **99**, 3454–3469.

Dalguer, L.A., Irikura, K., Zhang, W., & Riera, J.D., 2002. Distribution of Dynamic and Static Stress Changes during 2000 Tottori (Japan) Earthquake: Brief Interpretation of the Earthquake Sequences; Foreshocks, Mainshock and Aftershocks, *Geophys. Res. Lett.*, **29**, 5-1-5–4.

Day, S.M., 1982. Three-dimensional finite difference simulation of fault dynamics: Rectangular faults with fixed rupture velocity, *Bull. Seismol. Soc. Am.*, **72**, 705–727.

Day, S.M., Dalguer, L.A., Lapusta, N., & Liu, Y., 2005. Comparison of finite difference and boundary integral solutions to three-dimensional spontaneous rupture, *J. Geophys. Res. Solid Earth*, **110**, 1–23.

Di Toro, G., Han, R., Hirose, T., Paola, N. De, Nielsen, S., Mizoguchi, K., Ferri, F., Cocco, M., & Shimamoto, T., 2011. Fault lubrication during earthquakes, *Nature*, **471**, 494–498.

Dunham, E.M., & Archuleta, R.J., 2004. Evidence for a Supershear Transient during the 2002 Denali Fault Earthquake **94**, 256–268.

Fukuyama, E., 2003. Estimation of the Critical Slip-Weakening Distance: Theoretical Background, *Bull. Seismol. Soc. Am.*, **93**, 1835–1840.

Fukuyama, E., & Mikumo, T., 2007. Slip-weakening distance estimated at near-fault stations, *Geophys. Res. Lett.*, **34**, 2–6.

Fukuyama, E., & Suzuki, W., 2016. Near-fault deformation and Dc″ during the 2016 Mw7.1 Kumamoto earthquake, *Earth, Planets Sp.*, **68**, 6–11.

Galis, M., Pelties, C., Kristek, J., Moczo, P., Ampuero, J.-P., & Mai, P.M., 2015. On the initiation of sustained slip-weakening ruptures by localized stresses, *Geophys. J. Int.*, **200**, 888–907.

Goldsby, D.L., & Tullis, T.E., 2011. Flash heating leads to low frictional strength of crustal rocks at earthquake slip rates, *Science*, **334**, 216–218.

Goto, H., & Sawada, S., 2010. Trade-offs among dynamic parameters inferred from results of dynamic source inversion, *Bull. Seismol. Soc. Am.*, **100**, 910–922.

Guatteri, M., 2000. What Can Strong-Motion Data Tell Us about Slip-Weakening Fault-Friction Laws?, *Bull. Seismol. Soc. Am.*, **90**, 98–116.

Houston, H., 2015. Low friction and fault weakening revealed by rising sensitivity of tremor to tidal stress, *Nat. Geosci.*, **8**, 409–415.

Huang, Y., & Ampuero, J.P., 2011. Pulse-like ruptures induced by low-velocity fault zones, *J. Geophys. Res. Solid Earth*, **116**, 1–13.

Ida, Y., 1972. Cohesive force across the tip of a longitudinal-shear crack and Griffith's specific surface energy, *J. Geophys. Res.*, **77**, 3796–3805.

Ide, S., & Takeo, M., 1997. Determination of constitutive relations of fault slip based on seismic wave analysis, *J. Geophys. Res. Solid Earth*, **102**, 27379–27391.

Kaneko, Y., Fukuyama, E., & Hamling, I.J., 2017. Slip-weakening distance and energy budget inferred from near-fault ground deformation during the 2016 Mw7.8 Kaikōura earthquake, *Geophys. Res. Lett.*, **44**, 4765–4773.

Kaneko, Y., & Lapusta, N., 2010. Tectonophysics Supershear transition due to a free surface in 3-D simulations of spontaneous dynamic rupture on vertical strike-slip faults, *Tectonophysics*, **493**, 272–284.

Kurzon, I., Vernon, F.L., Ben-Zion, Y., & Atkinson, G., 2014. Ground Motion Prediction Equations in the San Jacinto Fault Zone: Significant Effects of Rupture Directivity and Fault Zone Amplification, *Pure Appl. Geophys.*, **171**, 3045–3081.

Ma, S., Custódio, S., Archuleta, R.J., & Liu, P., 2008. Dynamic modeling of the 2004 Mw 6.0 Parkfield, California, earthquake, *J. Geophys. Res. Solid Earth*, **113**, 1–16.

Mikumo, T., Olsen, K.B., Fukuyama, E., & Yagi, Y., 2003. Stress-breakdown time and slip-weakening distance inferred from slip-velocity functions on earthquake faults, *Bull. Seismol. Soc. Am.*, **93**, 264–282.

Nielsen, S.B., & Olsen, K.B., 2000. Constraints on Stress and Friction from Dynamic Rupture Models of the 1994 Northridge, California, Earthquake, *Pure Appl. Geophys.*, **157**, 2029–2046.

Olsen, K.B., Madariaga, R., & Archuleta, R.J., 1997. Three-dimensional dynamic simulation of the 1992 Landers earthquake, *Science*, **278**, 834–838.

Palmer, A.C., & Rice, J.R., 1973. The growth of slip surfaces in the progressive failure of over-consolidated clay, *Proc. R. Soc. London. A. Math. Phys. Sci.*, **332**, 527–548.

Reches, Z., & Lockner, D.A., 2010. Fault weakening and earthquake instability by powder lubrication, *Nature*, **467**, 452–455.

Spudich, P., 2005. The Effect of Bandwidth Limitations on the Inference of Earthquake Slip-Weakening Distance from Seismograms, *Bull. Seismol. Soc. Am.*, **94**, 2028–2036.

Tinti, E., Cocco, M., Fukuyama, E., & Piatanesi, A., 2009. Dependence of slip weakening distance (Dc) on final slip during dynamic rupture of earthquakes, *Geophys. J. Int.*, **177**, 1205–1220.

Tinti, E., Fukuyama, E., Piatanesi, A., & Cocco, M., 2005a. A Kinematic Source-Time Function Compatible with Earthquake Dynamics, *Bull. Seismol. Soc. Am.*, **95**, 1211–1223.

Tinti, E., Spudich, P., & Cocco, M., 2005b. Earthquake fracture energy inferred from kinematic rupture models on extended faults, *J. Geophys. Res.*, **110**, B12303.

Viesca, R.C., & Garagash, D.I., 2015. Ubiquitous weakening of faults due to thermal pressurization, *Nat. Geosci.*, **8**, 875–879.

Weng, H., & Yang, H., 2018. Constraining Frictional Properties on Fault by Dynamic Rupture Simulations and Near-Field Observations, *J. Geophys. Res. Solid Earth*, **123**, 6658–6670.

Weng, H., & Yang, H., 2017. Seismogenic width controls aspect ratios of earthquake ruptures, *Geophys. Res. Lett.*, **44**, 2725–2732.

Weng, H., Yang, H., Zhang, Z., & Chen, X., 2016. Earthquake rupture extents and coseismic slips promoted by damaged fault zones, *J. Geophys. Res. Solid Earth*, **121**, 4446–4457.

Wibberley, C.A.J., & Shimamoto, T., 2005. Earthquake slip weakening and asperities explained by thermal pressurization **436**, 689–692.

Wu, C., Peng, Z., & Ben-zion, Y., 2009. Non-linearity and temporal changes of fault zone site response associated with strong ground motion, *Geophys. J. Int.*, **176**, 265–278.

Xu, J., Zhang, H., & Chen, X., 2015. Rupture phase diagrams for a planar fault in 3-D full-space and half-space, *Geophys. J. Int.*, **202**, 2194–2206.

Yang, H., 2015. Recent advances in imaging crustal fault zones: a review, *Earthq. Sci.*, **28**, 151–162.

Yang, H., Duan, Y., Song, J., Tian, X., Yang, W., Wang, W., and Yang, J., 2020. Fine structure of the Chenghai fault zone, Yunnan, China constrained from teleseismic travel time and ambient noise tomography, *J. Geophys. Res.,* in revision.

Yang, H., Li, Z., Peng, Z., Ben-Zion, Y., & Vernon, F., 2014. Low-velocity zones along the San Jacinto Fault, Southern California, from body waves recorded in dense linear arrays, *J. Geophys. Res. Solid Earth*, **119**, 8976–8990.

Yang, H., Liu, Y., & Lin, J., 2013. Geometrical effects of a subducted seamount on stopping megathrust ruptures, *Geophys. Res. Lett.*, **40**, 2011–2016.

Yang, H., & Yao, S., 2019. In-situ frictional properties on seismogenic faults inferred from near-field observations and numerical simulations, in: EGU General Assembly 2019. p. 12466.

Yang, H., Yao, S., He, B., & Newman, A. V., 2019. Earthquake rupture dependence on hypocentral location along the Nicoya Peninsula subduction megathrust, *Earth Planet. Sci. Lett.*, **520**, 10–17.

Yang, H., & Zhu, L., 2010. Shallow low-velocity zone of the San Jacinto fault from local earthquake waveform modelling, *Geophys. J. Int.*, **183**, 421–432.

Yang, H., Zhu, L., & Cochran, E.S., 2011. Seismic structures of the Calico fault zone inferred from local earthquake travel time modelling, *Geophys. J. Int.*, **186**, 760–770.

Yao, S., and Yang, H., 2020. Rupture Dynamics of the 2012 Nicoya M_w 7.6 Earthquake: Evidence for Low Strength on the Megathrust, *Geophys. Res. Lett.*, revised.

Table 1. Parameters Setting in Homogenous Models

Fault parameters	**Value**
Nucleation Radius R_{nuc} (km)	4.00
Peak strength, τ_s (MPa)	31.40
Dynamic stress, τ_d (MPa)	27.00
Initial shear stress(nucleation), τ_0^i (MPa)	0.2+τ_s
Initial shear stress, τ_0 (MPa)	29.00
Slip-weakening distance, d_c (m)	0.40
Poisson's Ratio, ν	0.25
Density, ρ (g/cm^3)	2.705
V_p (km/s)	5.77
V_S (km/s)	3.33
μ (GPa)	30

Table 2. Application Cases of D_c'' Method

Earthquake & Station info	Magnitude	D_c''	Station off-fault distance	Total Slip	D_c''/Total Slip	Distance from epicenter	References
2000 Tottori	Mw 6.6	0.3 m	0.1 km	1 m	0.3	~ 4.7 km	(Mikumo et al., 2003; Fukuyama and Mikumo, 2007)
2002 Denali	Mw 7.9	2.5 m	3 km	6.5 m	0.38	~ 85 km	(Fukuyama and Mikumo, 2007)
2016 Kumamoto	Mw 7.1	1 m	0.5 km	~2.3 m	0.43	~ 7 km	(Fukuyama and Suzuki, 2016)
2016 Kaikoura	Mw 7.8	4.9 m	2.7 km	14 m	0.35	~ 115.6 km	(Kaneko et al., 2017)

Figures

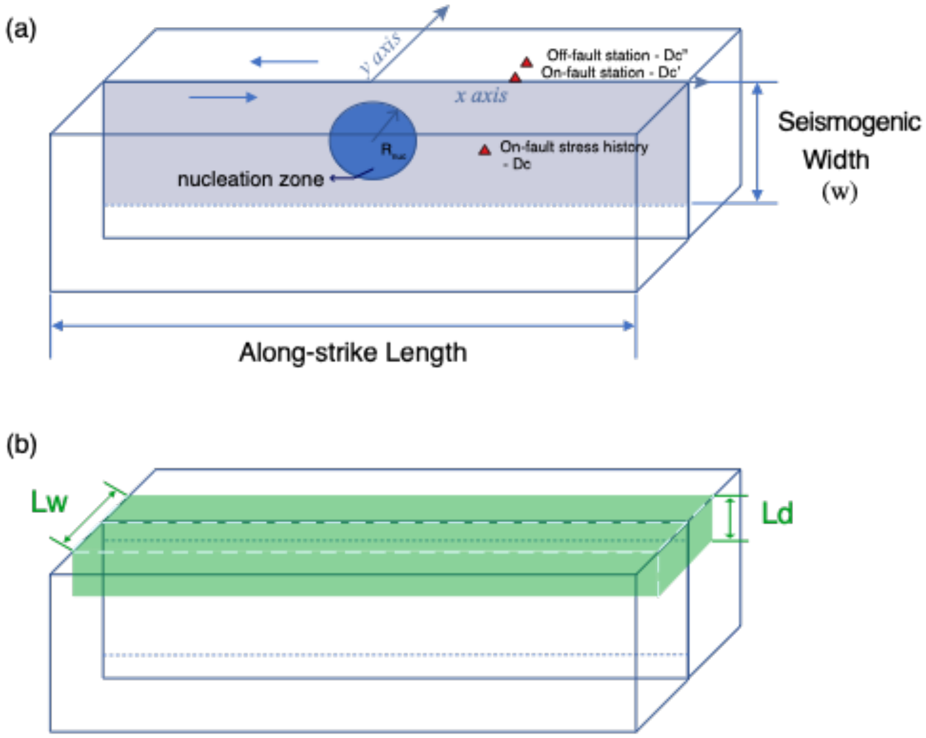

Figure 1. (a) Model setup of rupture simulation. We set left-lateral strike-slip fault model in this study. Navy circle in the center shows the nucleation zone location; light blue band indicates the seismogenic fault zone. The x, y axis corresponds to the ground coordinate axis used in the following D_c'' distribution figures. Red triangles represent virtual stations to infer D_c, D_c' and D_c'' respectively. (b) Illustration of the model with low-velocity zone. LVZ is shown in light green. L_w refers to the LVZ width in the fault-normal direction; L_d indicates the LVZ depth.

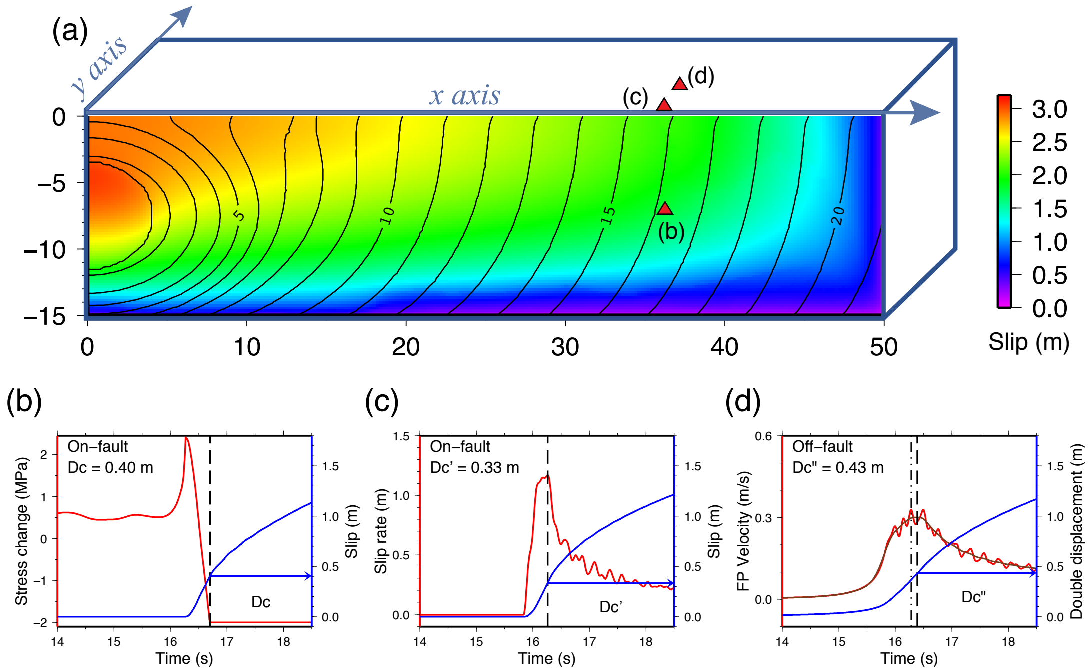

Figure 2. Illustration of determining D_c, D_c' and D_c''. (a) Cutting profile of slip on the fault plane of a uniform model with $w = 15\ km$. The contours are isochrones of rupture front. Red triangles correspond to the locations to obtain D_c, D_c' and D_c'' in subfigure (b), (c) and (d). (b) Stress (red) and slip (blue) history of the on-fault grid at $x = 36.4\ km, depth = -7.4\ km$. Dash line indicates the stress breakdown time and the corresponding slip value is D_c. (c) Time history of slip rate (red) and slip (blue) of the on-fault grid at $x = 36.4\ km, depth = 0\ km$. Dash line indicates the time of peak slip rate; D_c' is inferred at the corresponding slip value. (d) Time history of fault-parallel velocity (red) and displacement (blue). Amplitude of displacement is doubled for estimation of D_c'' in the strike-slip fault model. The brown curve shows the waveform with 2 Hz lowpass filter applied. The dash line and dot-dash line mark the peak velocity time of filtered waveform and raw data respectively. $D_c'' = 0.43m$ is obtained from the filtered data.

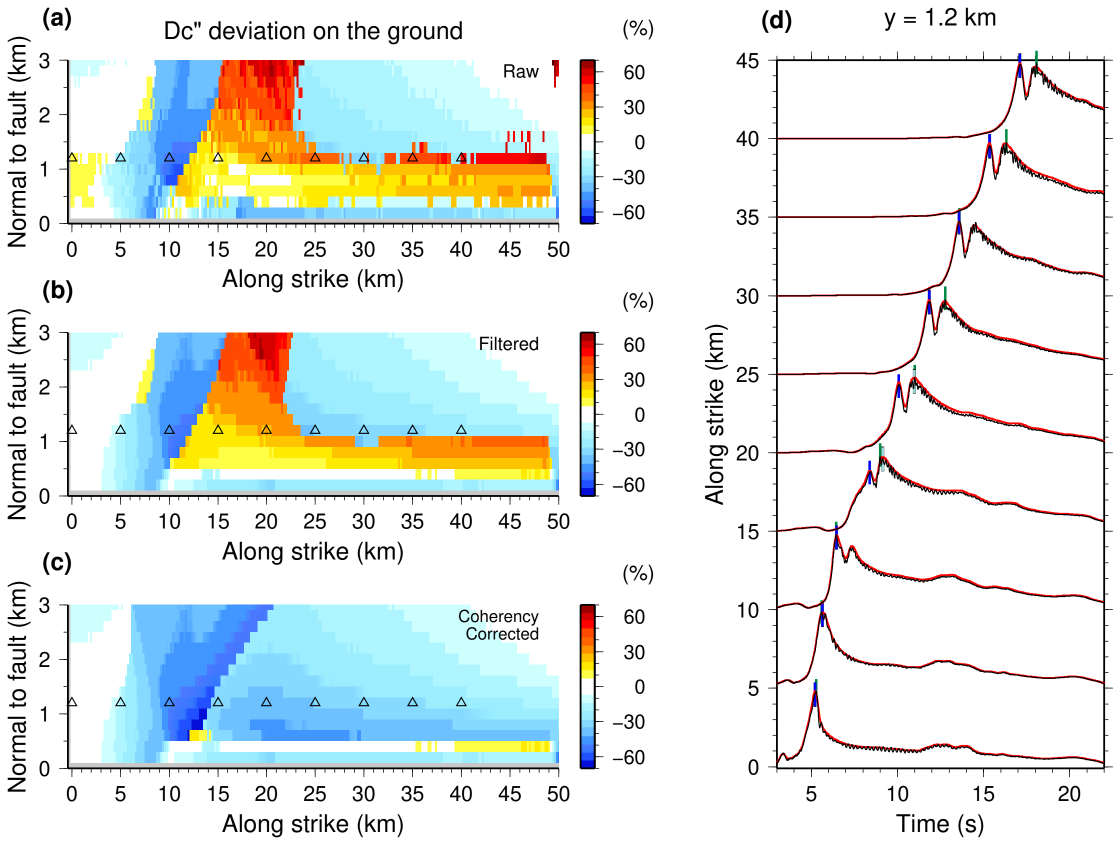

Figure 3. Data processing with filter and coherency correcting. (a) D_c'' deviation degree (i.e. $\frac{D_c''-D_c}{D_c}$, D_c is constant, 0.4 m) inferred from the raw data (corresponding to dark green time ticks in (d)). Triangles represent the virtual station locations of the profile shown in (d). (b) D_c'' deviation degree with filtered applied. The peak time to infer D_c'' is selected from 2 Hz lowpass filtered velocity waveforms (corresponding to light green time ticks in (d)). (c) D_c'' deviation degree after coherency correcting (corresponding to blue time ticks in (d)). (d) Fault-parallel velocity profile along strike direction (profile location at y = 1.2 km, shown as triangles in (a) to (c)). Red curves are 2 Hz lowpass filter velocity waveforms, beneath which black curves show the raw data. Blue ticks mark the picked time t_p to determine D_c'' after coherency correcting. Light green ticks show the time of maximum velocity from filtered data. Dark green ticks exhibit the time of maximum velocity from raw data. For the traces with ticks overlapped, the plotting order of ticks is raw (dark green), filtered (light green) then coherency corrected (blue).

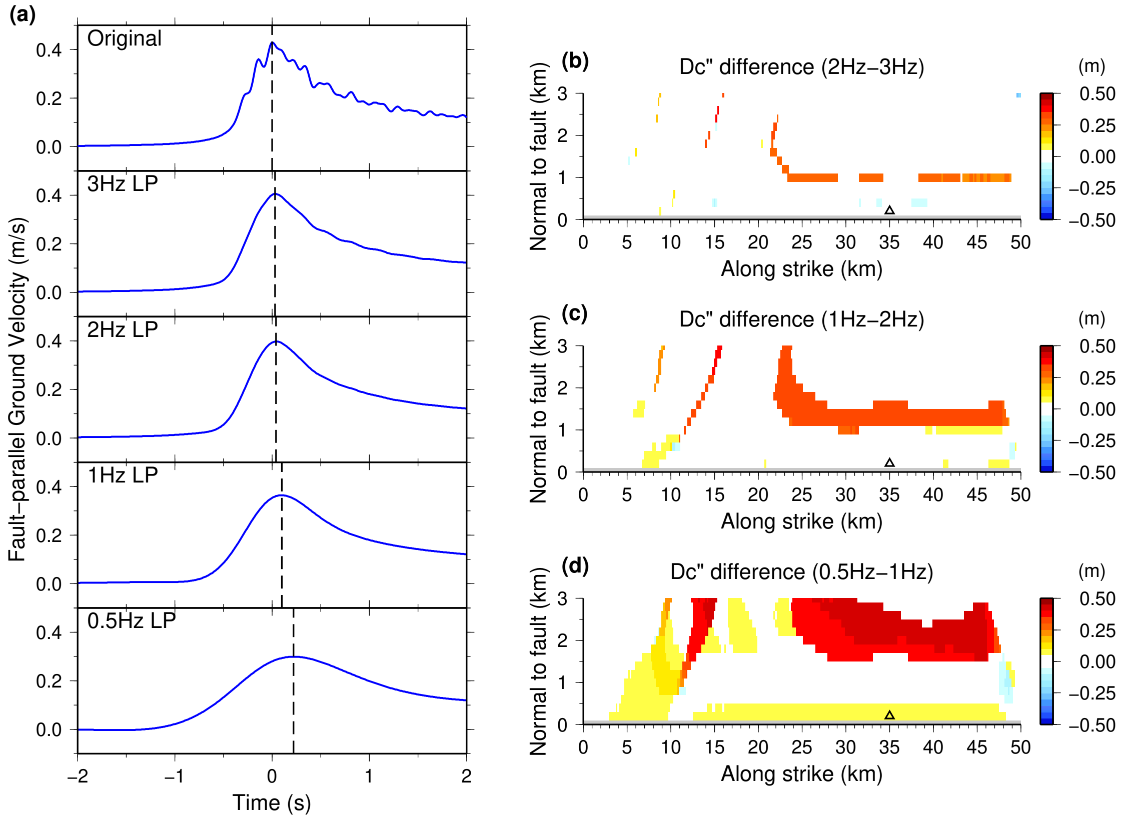

Figure 4. Comparison of different lowpass filter bands. (a) Original ground velocity waveform output from the model and lowpass filtered waveforms with cutoff frequency at 3 Hz, 2 Hz, 1 Hz and 0.5 Hz, respectively. Waveforms are extracted from the grid at $x = 35\ km, y = 0.2\ km$ (shown as triangles in (b)-(d)) of a uniform model with seismogenic width $w = 15\ km$. (b) Differences between D_c'' values with peak time obtained from 2 Hz & 3 Hz lowpass filtered waveforms. (c) and (d) are similar to (b), but the compared lowpass filters are 1 Hz & 2 Hz and 0.5 Hz & 1 Hz, respectively.

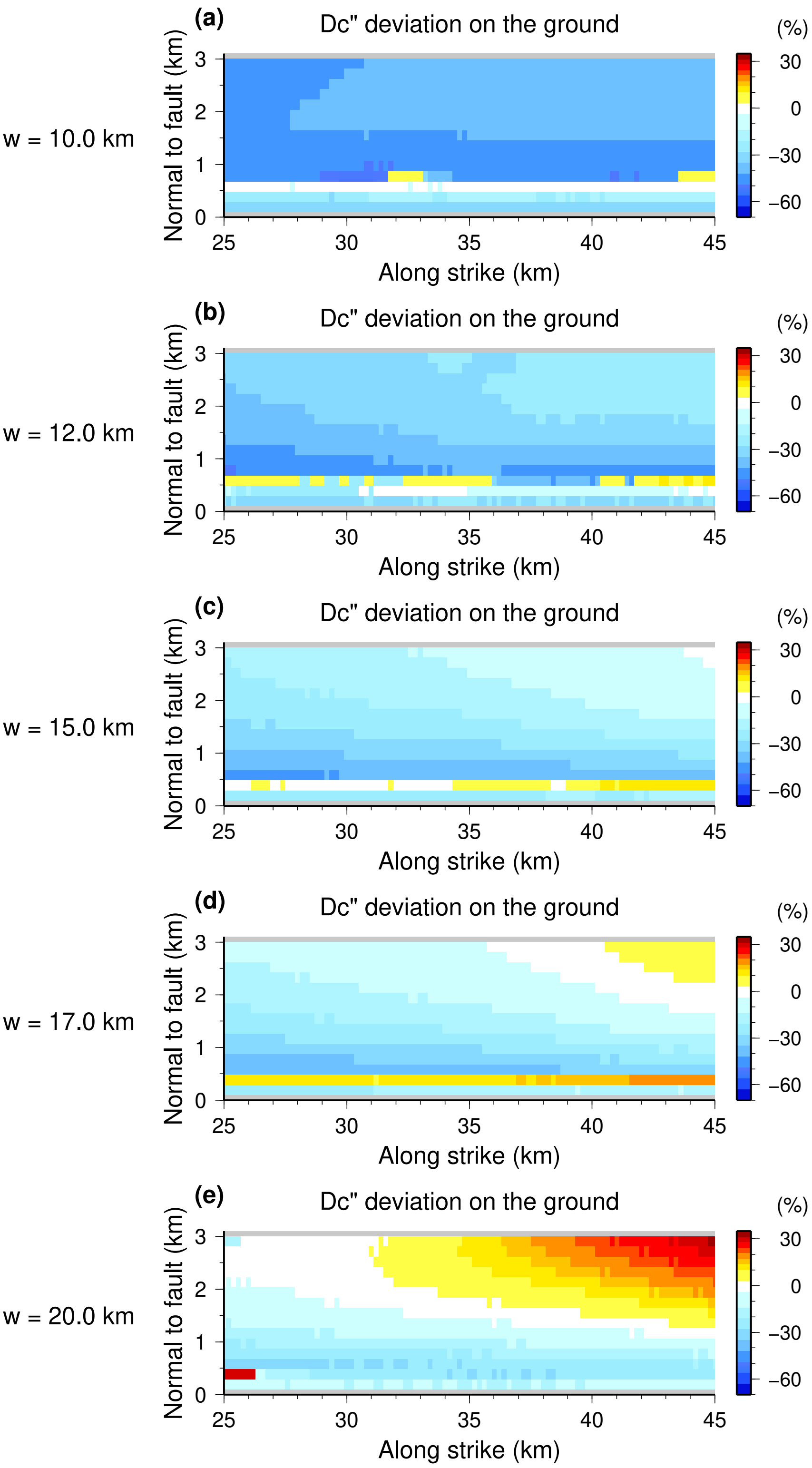

Figure 5. D_c'' deviation degree after filter and coherency correction applied in the selected region. (a) to (e) are of uniform models with seismogenic widths of 10 km, 12 km, 15 km, 17 km and 20 km, respectively.

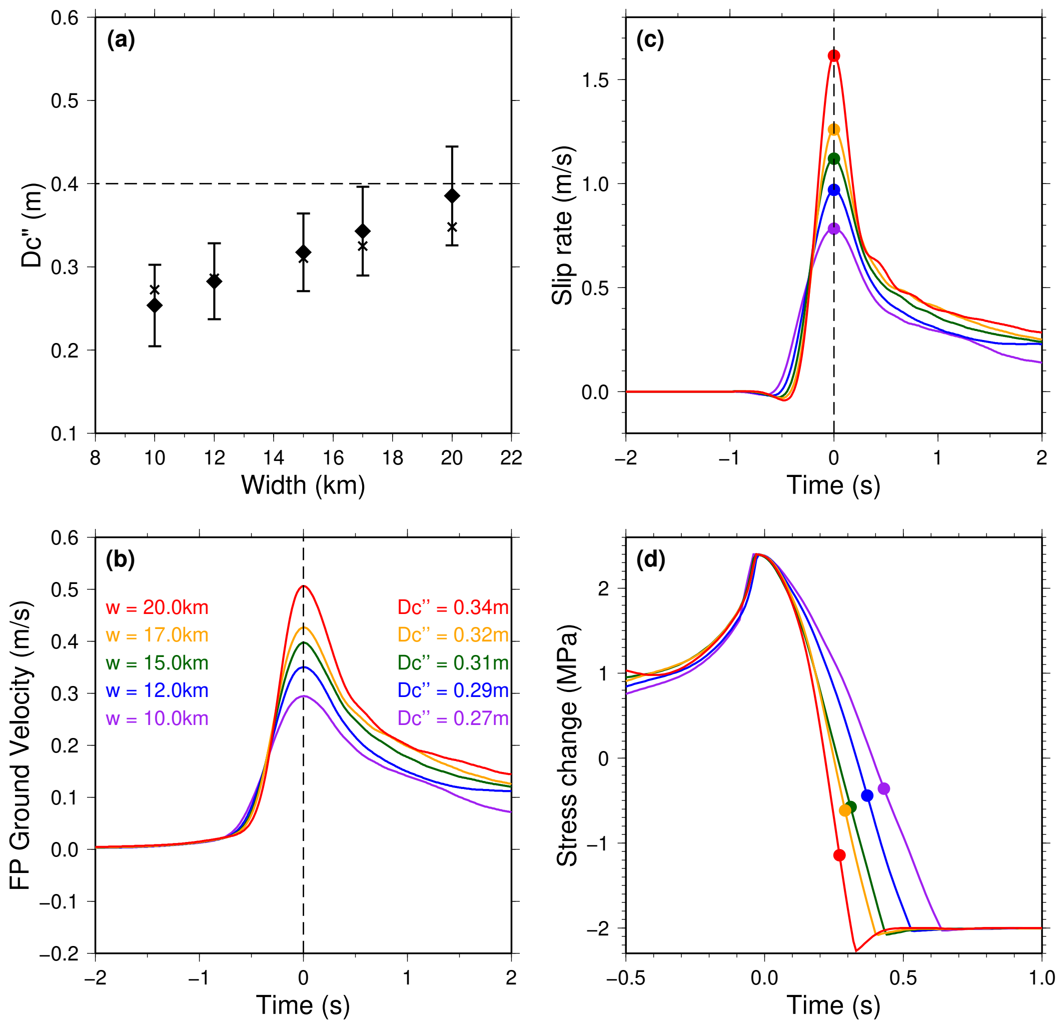

Figure 6. (a) Average D_c'' values versus seismogenic width in uniform models. Diamonds are the average D_c'' values calculated in the selected region shown in Fig. 5. Error bars for y axis indicate the standard deviations of D_c''. The crosses show the average d_c'' values of grids with off-fault distance y = 0.2 km. (b) Ground velocity waveforms from models with variant widths aligned at the peak velocity (extracting from a same position: x = 35 km, y = 0.2 km). (c) Slip rate time series from models with variant widths aligned at the peak slip rate (extracting from: x = 35 km, z = 0 km). 2 Hz lowpass filter is applied on waveforms in (b) & (c). (d) Shear stress time evolution aligned with the peak strength. Solid dots denote the time of peak slip rate as shown in (c). Color legends of waveforms is shown in (b) corresponding to the widths.

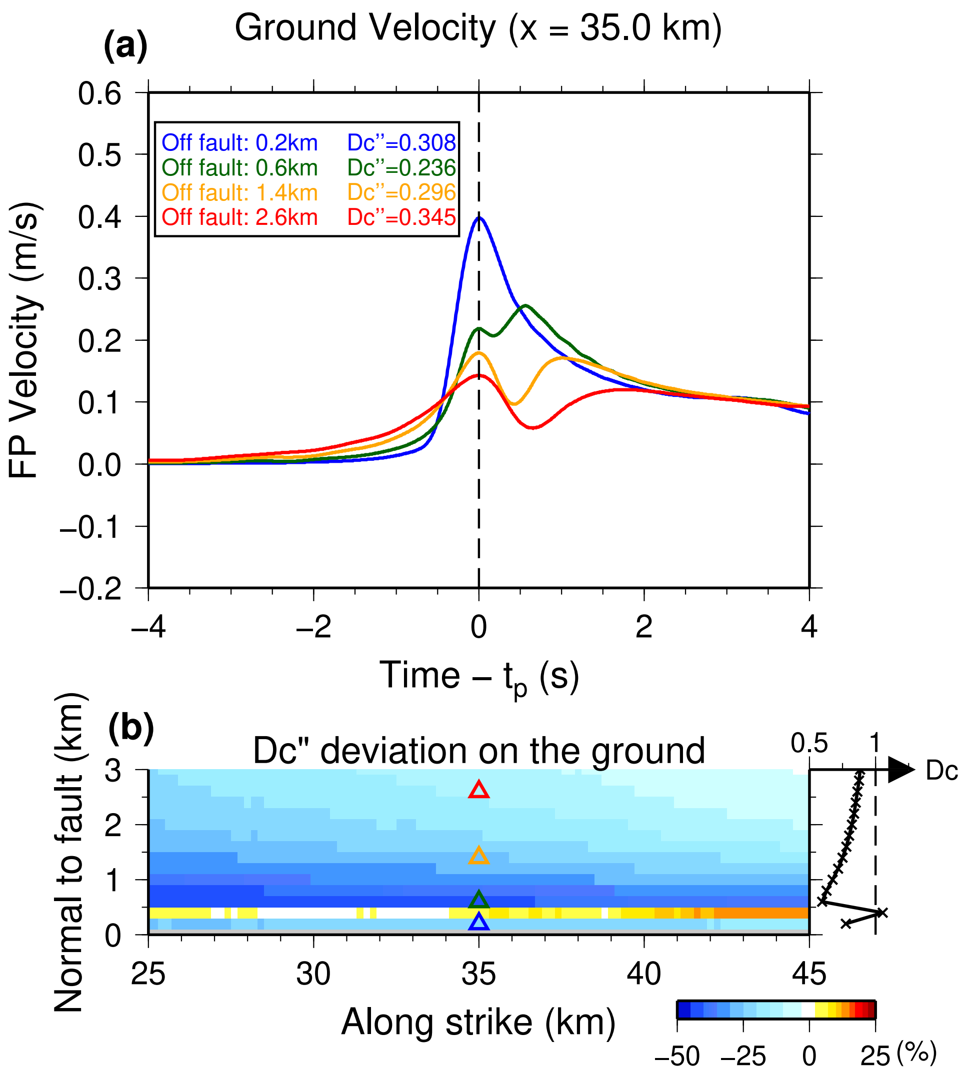

Figure 7. (a) Velocity waveforms variation in fault-normal direction. The fault-parallel velocity waveforms are aligned at the picked time t_p and are from four grids with different fault-normal distances (x = 35 km). The off-fault distances and corresponding D_c'' values are shown in the legend. 2 Hz lowpass filter is applied on waveforms. (b) Ground distributions of D_c'' deviation degree. Triangles represent the locus of the four selected grids in (a). The colors of triangles and waveforms are corresponding to each other. The crosses and the line on the right of (b) show the average D_c'' trend in the fault-normal direction.

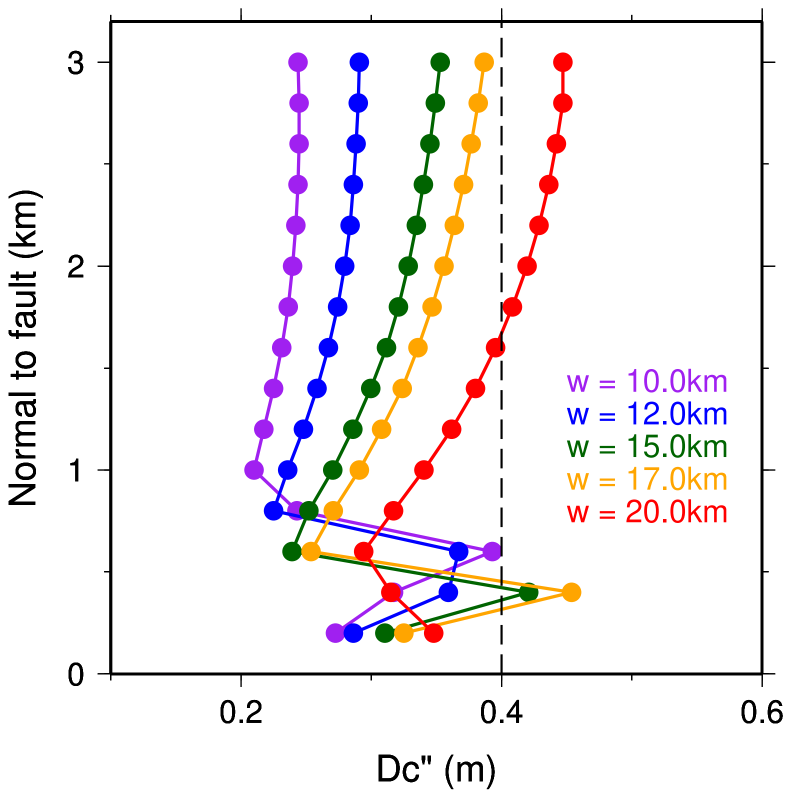

Figure 8. Average D_c'' trend in the fault-normal direction. Each color corresponds to a seismogenic width. Solid circle on the lines represent an average D_c'' value calculated in a fault-normal distance. The dash line shows the prescribed $D_c = 0.4\ m$.

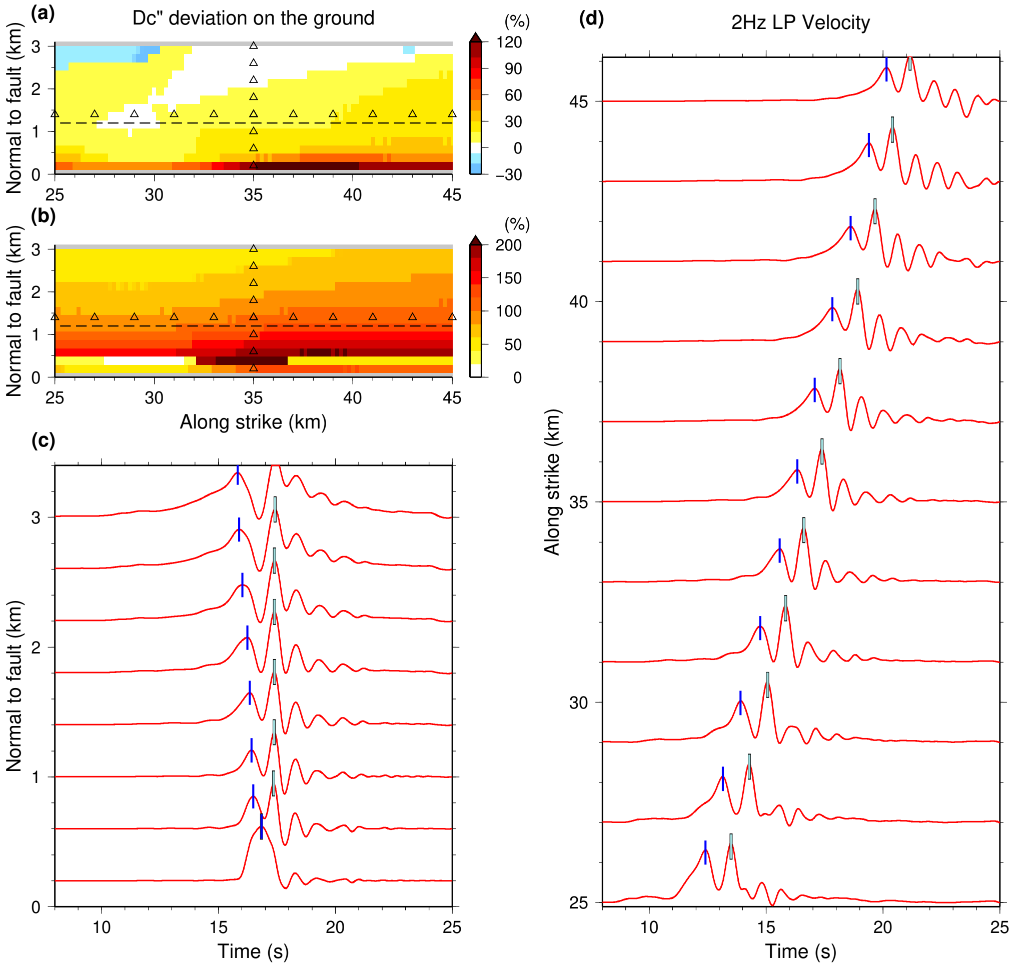

Figure 9. D_c'' deviation and waveform profiles in a LVZ model ($L_w = 2.4\ km,\ L_d = 3.0\ km$, velocity reduction is 30%). (a) D_c'' deviation degree inferred from first rupture-related velocity peak after coherency correction. (b) D_c'' deviation degree obtained at the maximum fault-parallel ground velocity time. The dash line in (a) and (b) marks the one-side range of LVZ on the ground Triangles in (a) & (b) show the station locations of profiles in (c) & (d). (c) Fault-parallel ground velocity profile along fault-normal direction (profile location at $x = 35.0\ km$ from initial zone). (d) Fault-parallel ground velocity profile along strike direction (profile location at y = 1.4 km off the fault trace). In subfigure (c) & (d), waveforms in red are 2 Hz lowpass filtered fault-parallel velocities. Blue ticks mark the picked time t_p after coherency correcting to determine D_c'' in (a). Light green ticks show the time of maximum velocity in the waveforms, which leads to a distribution of D_c'' in (b).

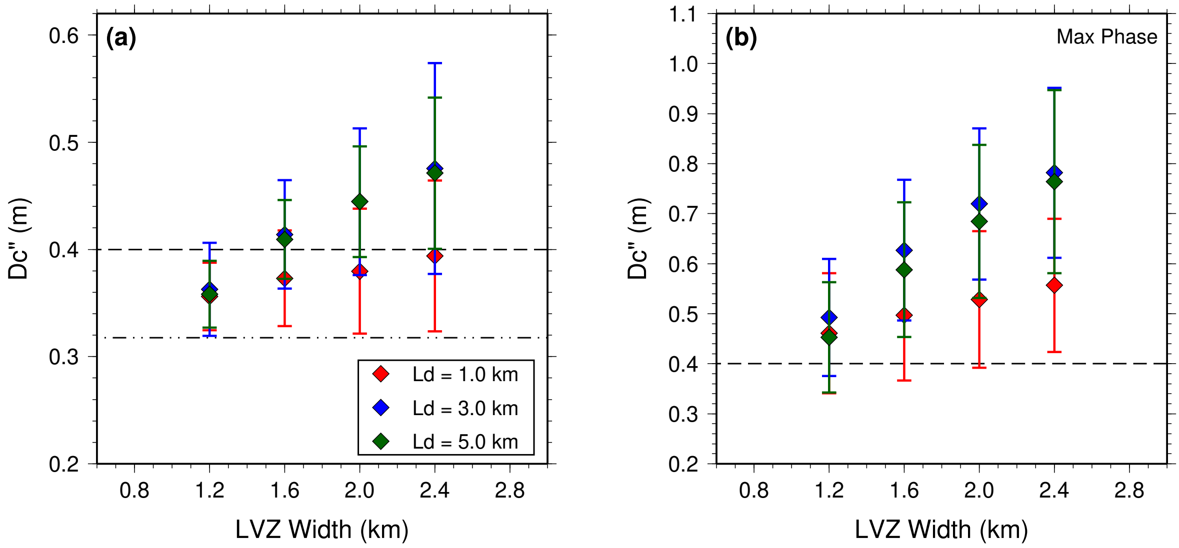

Figure 10. Average D_c'' values versus L_w. D_c'' values in (a) are obtained using the first rupture-related velocity peak after coherency correcting (similar to Fig. 9a). D_c'' in (b) are obtained at the maximum fault-parallel ground velocity time (similar to Fig. 9b). Red, blue and green diamonds represent models with $L_d = 1.0\ km, 3.0\ km\ and\ 5.0\ km$, respectively. The dash line marks the prescribed constant $D_c = 0.4\ m$. The dot dash line shows the average D_c'' value in the uniform model without LVZ.

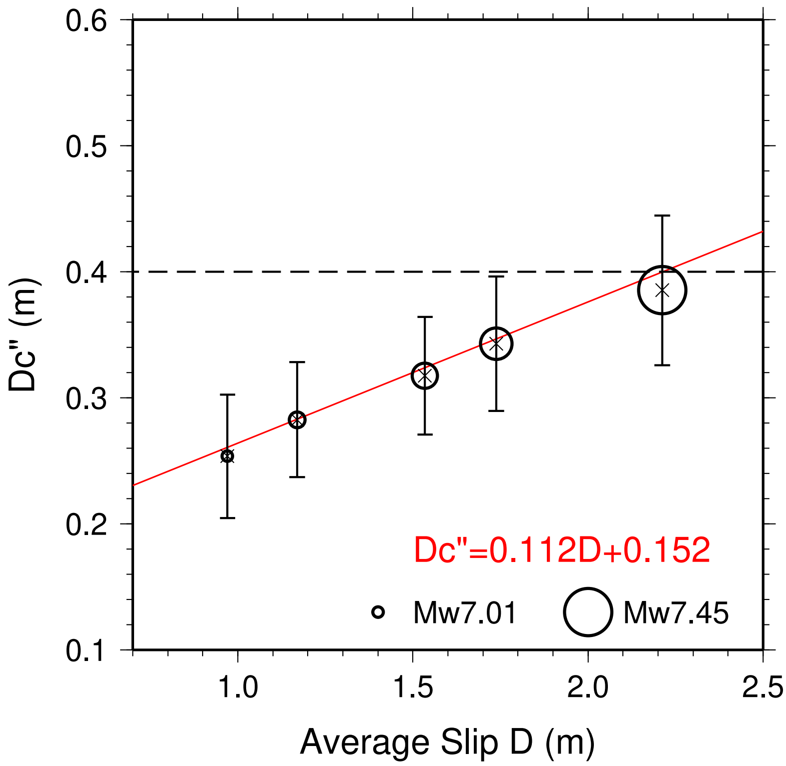

Figure 11. Average D_c'' values versus slip in uniform models. Radius of the circles corresponds to the magnitude of the scenario earthquakes. Red line shows the least square fitting of the data points, with the expression equation shown in red. The dash line marks the prescribed constant $D_c = 0.4\ m$.